PHYSICAL REVIEW A VOLUME 46, NUMBER 7 1 OCTOBER 1992

Excitation of target Auger-electron emission by the impact of highly charged ions: N^{6+}, O^{7+}, and Ne^{9+} on Pt(110)

S. Schippers,* S. Hustedt, and W. Heiland
Universität Osnabrück, D-4500 Osnabrück, Germany

R. Köhrbrück
Hahn-Meitner-Institut Berlin, D-1000 Berlin 39, Germany

J. Bleck-Neuhaus
Universität Bremen, D-2800 Bremen, Germany

J. Kemmler
Centre Interdisciplinaire de Recherche avec les Ions Lourds, F-14040 Caen CEDEX, France

D. Lecler and N. Stolterfoht*
Laboratoire de Spectroscopie Atomique, ISMRa Université Caen, F-14021 Caen, France

(Received 10 April 1992)

We studied the interaction of highly charged ions on metal surfaces leading to the emission of electrons from the projectile and from the target. The target electrons are due to potential emission, kinetic emission, and Auger-electron emission. In our electron spectra two types of target Auger electrons are distinguished. Electrons near 135 and 220 eV are ascribed to Pt $N_{45}O_1O_{23}$ and $N_{45}N_{67}V$ Auger transitions. They are caused by K-vacancy transfer into the Pt N shell and are only emitted under bombardment with N^{6+} and O^{7+}. The other type of electrons near 40 and 60 eV are ascribed to Pt $O_{23}VV$ and $N_{67}VV$ Auger transitions. They are due to direct ionization and are emitted under bombardment with each projectile used. According to our analysis, the initial projectile K-shell vacancy survives the transport to and at least 8×10^{-16} s within the target surface.

PACS number(s): 79.20.Nc, 34.70.+e, 79.90.+b

I. INTRODUCTION

The first energy-resolved secondary-electron spectra due to the impact of highly charged ions revealed Auger-electron emission from the projectile and from the target [1, 2]. The projectile Auger emission is the subject of many studies (see reviews [3, 4]). Target Auger emission has been reported for different cases, besides the $N^{6+} \rightarrow$ C, Au and $O^{7+} \rightarrow$ Au [1, 5, 6], for C^{5+}, N^{6+}, $Ar^{9+} \rightarrow$W [2, 7] and N^{6+}, $O^{7+} \rightarrow$ C [8]. It is generally accepted that the Auger emission from the target atoms is due to the transfer of a projectile vacancy into an inner shell of a target atom in a Landau-Zener-type process. Other possibilities for target Auger emission are the transfer ionization [7, 9] and the direct ionization. In a transfer ionization process two electrons in the target atom are excited. One electron fills the hole in the projectile atom and the other electron is emitted, i.e., an interatomic Auger capture occurs. The direct ionization is due to the promotion of target electrons in the collision to energies above the vacuum level.

The analysis of these inner-shell processes is important for the whole scenario, since the number of Auger electrons emitted from the target is in our experiments comparable to the number of projectile KLL Auger electrons. The analysis of the target Auger emission will give further insight into the time scales of the capture processes into the projectile and the time scales of the internal deexcitation processes of the projectiles. In order for a vacancy transfer to occur the projectile K-shell vacancies have to survive up to a certain internuclear distance to at least surface atoms or deeper layer atoms of the solid. Estimates of the (classical) trajectories of the projectiles and of the escape depth of the target electrons [10] allow conclusions about the depth of origin of the target electrons.

Here we decribe the results of the interaction of N^{6+}, O^{7+}, and Ne^{9+} with a clean Pt(110) surface. The target has been chosen because a well-defined Pt(110) surface can be prepared and maintained without too much effort. The projectiles used differ from each other especially in that the energetic position of the nitrogen, oxygen, and neon K shells are different with respect to the platinum N-shell levels. They lie above, in between, and below the platinum N shell, respectively.

We study angular-resolved electron spectra for projectile energies of 60 keV, 70 keV, and 90 keV, respectively. When varying the observation angle of the electrons discrimination between target and projectile emission is possible. Since the projectile emission occurs from a moving source the energy of, e.g., the projectile KLL Auger lines shows an apparent dependence on the electron observation angle. The target Auger lines are found at fixed energies since they are emitted from atoms at rest. The analysis of the dependence on the type of projectile and on the impact angle of the ions leads to a different interpretation of the target Auger lines: the K-shell vacancies of the N^{6+} and O^{7+} projectiles are transferred into the N_{123} subshells of the platinum target by a Landau-Zener process. For Ne^{9+} this process is not possible because the neon K shell is energetically too low compared to the platinum N shell. Consequently no target Auger electrons due to platinum N-shell vacancies are found when using Ne^{9+} as a projectile.

II. EXPERIMENT

The experiments are performed in an ultrahigh-vacuum (UHV) system designed for angular-resolved electron spectroscopy at solid surfaces. The vacuum chamber (Fig. 1) has two sections, the upper one being a "service section" and the lower a μ-metal shielded "spectroscopy section." The service includes presently an ion gun (3M) for target cleaning. In connection with the electrostatic analyzer (ESA) the ion gun affords surface chemical analysis by ion scattering spectrometry (ISS) [11]. Figure 2 shows ion scattering (IS) spectra from contaminated and clean Pt(110). The target surface structure can be judged from low-energy electron diffraction (LEED) patterns using a "reverse view" LEED system (Omicron).

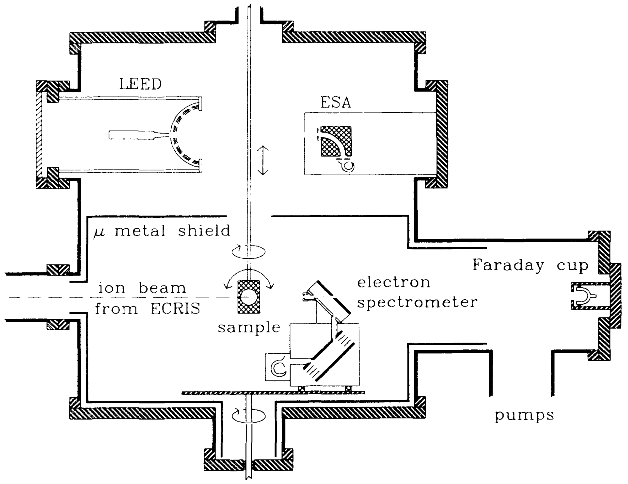

FIG. 1. Scheme of the UHV system (section). Not shown are the pumps (titanium sublimator and turbomolecular), the manipulator head providing the lift positioning and rotation of the target, the ion gun for sputtering and ion scattering spectroscopy (ISS), and the electron gun for testing the electron spectrometer and monitoring the target cleanliness by Auger-electron spectroscopy (AES). The upper half of the chamber equipped with LEED and ISS using the electrostatic analyzer (ESA) serves as the target preparation and analysis. In the lower half, shielded by an internal μ-metal chamber, secondary-electron spectra excited by the beam from the ECRIS or by the built-in electron gun are measured with the rotatable electron spectrometer.

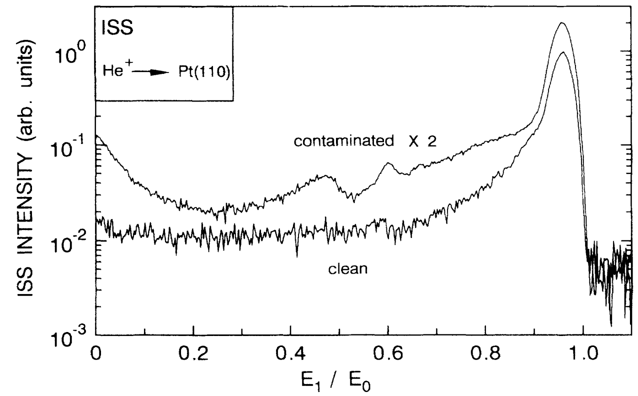

FIG. 2. IS spectra from Pt(110) before and after sputter cleaning (note the logarithmic intensity scale). The ordinate is the ratio between the kinetic energies of the He^+ ion before and after reflection from the surface.

In the spectroscopy section a tandem parallel-plate electron-energy analyzer [12] is mounted on a rotatable feedthrough such that angular-resolved energy spectra can be measured in an angular range of 0° to 180°. The energy resolution of the spectrometer as used here is $\Delta E/E = 2.5\%$. The energy resolution has been checked using an electron gun and measuring the elastic peak as a function of the primary energy. The spectroscopy section is screened against magnetic fields by an inner μ-metal chamber. The field inside the section is of the order of 10 mG. Figure 3 shows an electron generated secondary electron spectrum. The absence of C and O Auger lines is further proof of the target cleanliness. Only target Auger lines become visible after background subtraction as shown in the inset of Fig. 3.

The experiments were performed at the test bench of

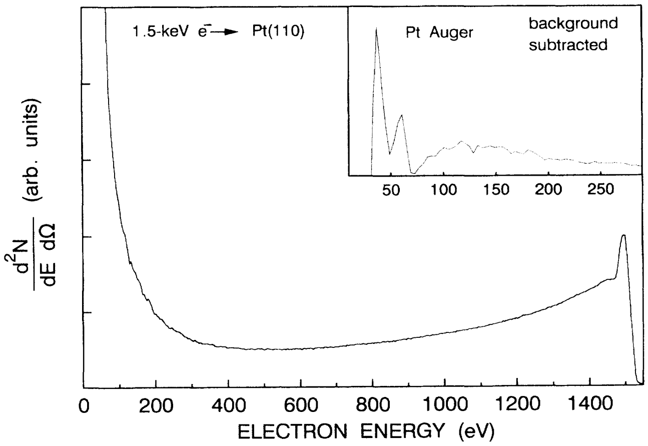

FIG. 3. Electron excited electron spectrum measured in the lower chamber [corrected for analyzer transmission function, linear intensity scale, angle of incidence (glancing) $\phi = 45°$, and angle of the detector with respect to the beam direction $\theta = 90°$]. The inset shows target Auger lines obtained after background subtraction.

the 14-GHz electron cyclotron resonance (ECR) source at the Grand Accelerateur National des Ions Lourds (GANIL), Caen, France. Mass- and charge-selected beams of N^{6+}, O^{7+}, and Ne^{9+} were used with currents of 150 nA, 60 nA, and 15 nA, respectively.

The target, Pt(110), is mounted on a two-axis goniometer. In the present study only the glancing angle was varied. With respect to the crystallographic directions a "random" azimuthal angle was chosen, in order to minimize channeling effects. The azimuthal angle is 18° off the [1$\bar{1}$0] direction of the Pt(110) surface. The target is heated for annealing and for thermal desorption of, e.g., H, H_2O, and CO. For the heating serves the usual electron beam heating device of the goniometer (Fisons).

III. RESULTS

Electron spectra for N^{6+}, O^{7+}, and Ne^{9+} ions incident on the Pt(110) surface are shown in Fig. 4 for $\psi = 10°$ glancing angle, $\theta = 120°$ observation angle (position of the electron analyzer with respect to the beam direction), and kinetic energy of the ions of 60 keV, 70 keV, and 90 keV, respectively. The electron yield scale is logarithmic; the spectra exhibit the following features. (i) There is the background due to kinetic electron emission—i.e., target electron emission caused by the transfer of kinetic energy from the projectile to target electrons—and "true" secondary-electron emission extending from low energies up to the region of the projectile *KLL* emission. (ii) The peaks at 340 eV, 450 eV, and 740 eV, respectively, are due to the projectile *KLL* emission. Correspondingly evidence for projectile *LMM* emission is found at low energies too. (iii) The N^{6+} and O^{7+} spectra have Pt Auger lines at 40 eV and 60 eV, and at 135 eV, and 220 eV, respectively, which clearly can be distinguished after subtraction of the background due to kinetic emission (Fig. 5). With Ne^{9+} the 135-eV and 220-eV lines are not detectable.

Before background subtraction the spectra have been corrected for channeltron electron detection efficiency, analyzer transmission, and geometrical factors. The method of background subtraction is suggested by the finding that the background is almost linear in a log-log plot (Fig. 6). We approximate the background by a fourth-power polynomial (Fig. 6). A similar observation and background treatment was made by Meyer *et al.* [6]. It is also possible to use a scaled N^{4+} spectrum to simu-

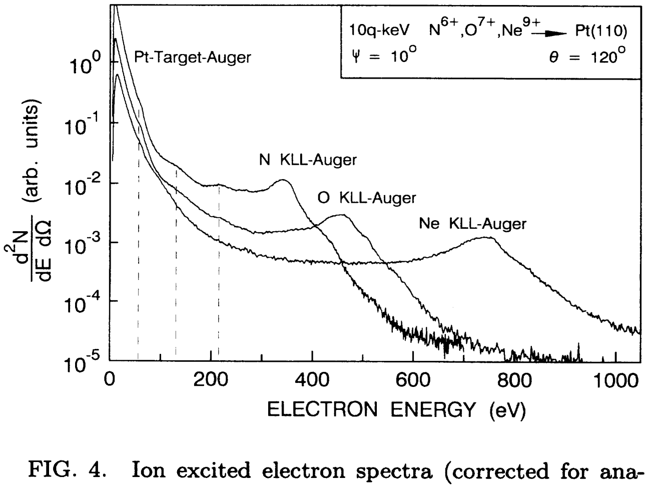

FIG. 4. Ion excited electron spectra (corrected for analyzer transmission function and logarithmic intensity scale).

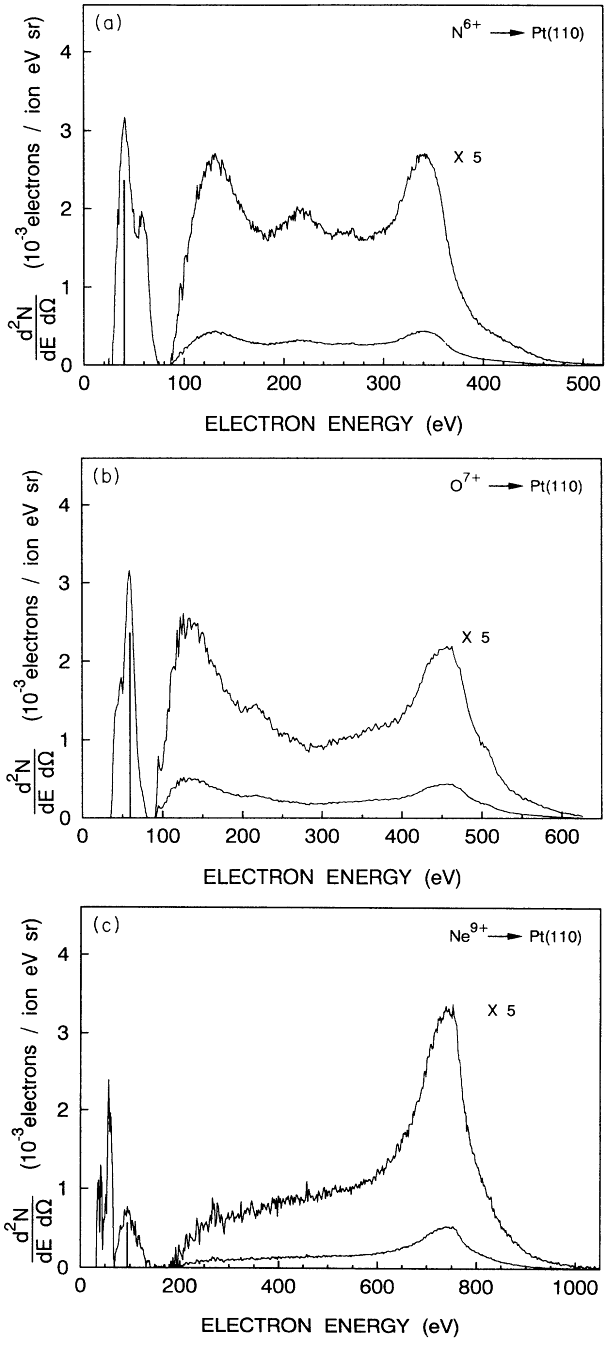

FIG. 5. Data as in Fig. 4 after background subtraction. The disappearance of the 135-eV and 220-eV Pt Auger peaks in the Ne^{9+} spectrum is significant. Going from N to Ne the projectile *LMM* Auger peaks (denoted by the vertical bars) shift through the target Auger peaks at 40 eV and 60 eV. The projectile *KLL* Auger peaks are at 340 eV, 450 eV, and 740 eV, respectively.

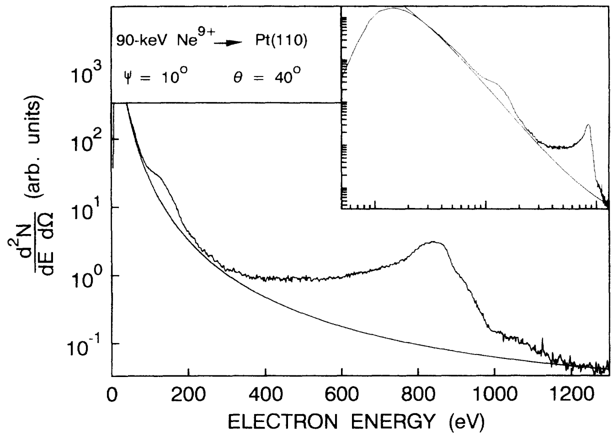

FIG. 6. Example of background treatment. The background is fitted as a fourth-order polynomial in the double-logarithmic plot (inset). The fit can also be judged from the semilogarithmic representation.

late the "background," i.e., to obtain an estimate of the kinetic emission. With N^{4+} neither projectile nor target Auger electrons are produced [13] within the energy range of interest.

After background subtraction it becomes clear that the main target Auger contributions are the 40-eV and 60-eV lines. The energetic position of these lines is in agreement with that of electron induced Auger spectra (Fig. 3). The projectile *LMM* Auger electrons are also found in this energy region. The *LMM* peaks shift to higher energies when going from nitrogen to neon. For nitrogen and oxygen the projectile *LMM* and the target Auger peaks at 40 eV and 60 eV overlap [Figs. 5(a) and 5(b)]. Whereas, for neon the projectile *LMM* structure appears at sufficiently high energies to be well separated from the target Auger lines at 40 eV and 60 eV [Fig. 5(c)]. For oxygen we also find a weak target Auger structure at 370 eV [Fig. 5(b)].

Table I lists the yield per incident ion of the projectile *KLL* Auger electrons and of the high energy (> 100 eV) target Auger electrons. The yields have been obtained by integrating the appropiate parts of the spectra shown in Fig. 5. Since the projectile *KLL* peaks of nitrogen and oxygen overlap in parts with the target Auger peaks we scaled the neon *KLL* Auger peak in order to separate the projectile and target Auger emission in the nitrogen and oxygen spectra. The corrected Ne^{9+} induced spectrum [Fig. 5(c)] shows the neon *KLL* Auger peak at 740 eV and the long low-energy tail due to electron-scattering and solid-state effects. This part of the spectrum is apparently not disturbed by target Auger peaks. For oxygen on the low-energy tail of the projectile *KLL* Auger emission the target Auger line at 370 eV is superimposed [Fig. 5(b)].

The scaling of the neon *KLL* peak does not take into account solid-state effects which certainly influence the shape of the projectile *KLL* peaks. When going from nitrogen to neon the energy of the projectile *KLL* Auger electrons increases (Fig. 5). Within the corresponding energy range the escape depth of electrons emitted from inside the target surface increases with increasing electron energy [10]. Hence among the projectile *KLL* electrons of the projectiles used the neon *KLL* Auger electrons are least and the nitrogen *KLL* Auger electrons are most absorbed within the solid. A proper scaling procedure of the neon *KLL* peak would have to account for the differences in absorption. However they certainly are of minor importance since the electron escape depth varies only about 10% over the energy range under consideration. Even within these uncertainties the numbers presented in Table I clearly confirm that besides projectile *KLL* Auger-electron emission, high-energy (> 100 eV) target Auger-electron emission also contributes significantly to the measured nitrogen and oxygen spectra. The line intensities listed in Table I suggest that the two processes are competing. There is no extra intensity resulting from target Auger emission, i.e., in the oxygen and nitrogen spectra the sum of the intensities from both processes does not exceed the neon *KLL* intensity.

A second set of experimental data is shown in Fig. 7. The electron energy spectra show that the target Auger emission vanishes with increasing glancing angle ψ. From $\psi = 10°$ to 90° the energy perpendicular to the surface is varied from 2 keV to 70 keV. We find no evidence for a kinematic shift of the high-energy Pt Auger lines which might be expected, e.g., for $\psi = 10°$. For such grazing angles it is possible to produce Pt recoils with an energy of 20 keV or a velocity of $\frac{1}{7}$ of the oxygen velocity of $v \simeq 9 \times 10^7\ \mathrm{cm\,s^{-1}}$. For this velocity we estimate for the 220-eV Pt line a shift of 12 eV. However, no such shift is found, which would be detectable in our experiment [Fig. 8(a)]. Possibly the Pt atoms emitting the 220-eV Auger lines have an isotropic velocity distribution so that no kinematic shift is measured. However, a kinematic broadening corresponding to that may contribute to the line shape. The spatial intensity distributions of the Pt Auger lines, which are peaked towards the surface normal ($\theta = 100°$), confirm this conclusion [Figs. 8(a) and 8(b)].

TABLE I. Projectile *KLL* and high-energy target Auger-electron yield for $10q$-keV N^{6+}, O^{7+}, and Ne^{9+}, glancing angle $\psi = 10°$, and electron observation angle $\theta = 120°$.

	Yield of projectile *KLL* electrons	Yield of Pt Auger electrons ($E > 100$ eV) (electrons per ion)	Sum of preceding columms
Ne	0.132		0.132
O	0.072	0.053	0.125
N	0.049	0.044	0.093

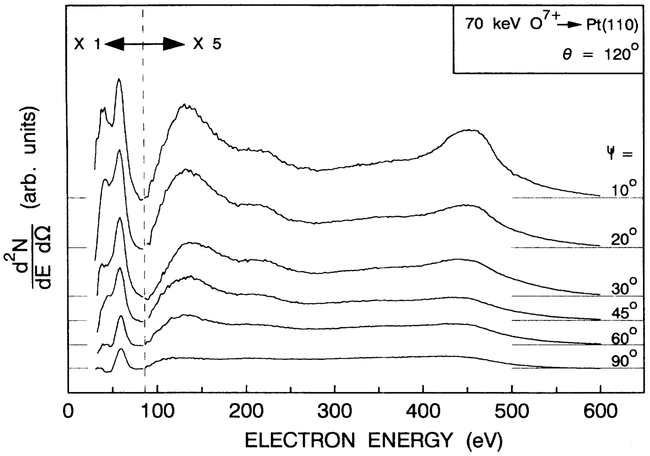

FIG. 7. The dependence of the Pt Auger-electron intensity on the glancing angle in background corrected spectra.

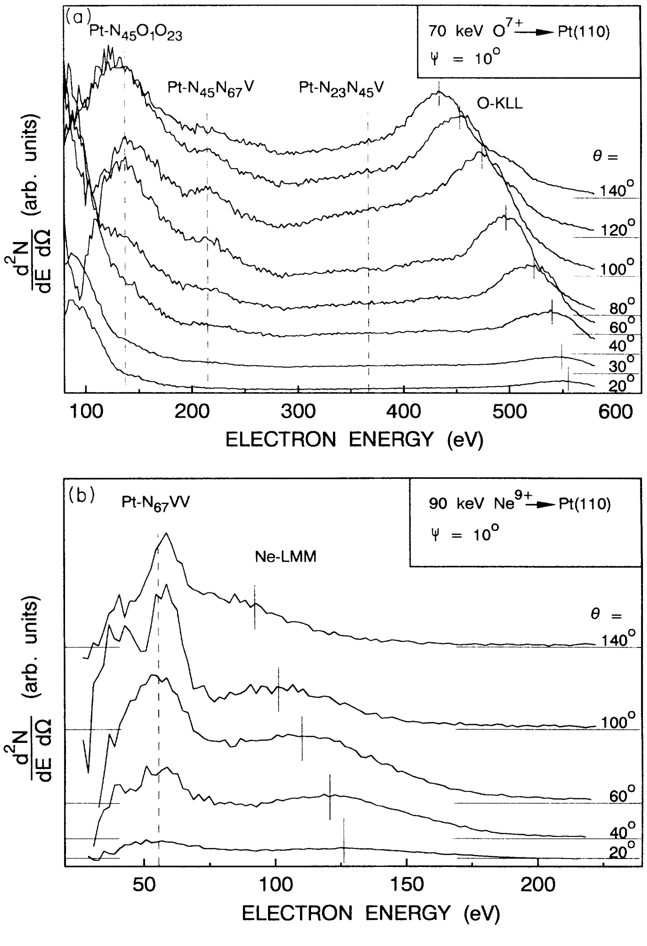

FIG. 8. The dependence of the Pt Auger-electron intensity on the angle θ of the detector. The angle θ is measured with respect to the beam direction. Note the kinematic shifts of the O *KLL* and the Ne *LMM* peaks, which have the same direction. Not fully seen is the O *LMM* line shifting also in this direction. The projectile lines are emitted essentially on the inward part of the trajectory; the target Auger lines are emitted from Pt atoms at rest.

They indicate the dependence of the electron yield on the electron observation angle θ at a fixed impact angle. In particular Fig. 8(b) shows the 40-eV and 60-eV Pt Auger lines and the neon *LMM* lines which are clearly separated in this case in contrast to the nitrogen and oxygen cases. In the latter cases the *LMM* lines "shift through" the Pt lines such that an analysis of the kinematic shift of the Pt lines is difficult. In the neon case [Fig. 8(b)] the energy of the Pt line shifts slightly to higher energies at high values of θ which would indicate emission from sputtered Pt atoms [14, 15]. The important observation is that Ne^{9+} produces only the low-energy Pt Auger lines and not the lines at 135 eV and 220 eV, even though in our experiment Ne^{9+} has a higher kinetic energy compared to N^{6+} and O^{7+}.

A further finding in our experiments is that both the yield of the target Auger electrons and the yield of the O^{7+} *KLL* projectile electrons (Fig. 7) decrease with increasing glancing angle. In our experiments the same behavior has also been found for the N^{6+} projectile. This observation implies that the target Auger electrons are induced by the *K* vacancies of the N^{6+} and O^{7+} projectiles.

IV. DISCUSSION

Details of the analysis of the *KLL* and *LMM* Auger emission of the projectiles are planned to be published elsewhere [16]. Transfer ionization can be excluded as the underlying mechanism for target electron emission. Since with transfer ionization one projectile level is also involved one would expect a shift in the associated electron emission energies depending on the projectile used [9]. Such a shift is not observed. In the N^{6+} and O^{7+} spectra [Figs. 5(a) and 5(b)] the peaks associated with target electron emission appear at the same energies. Hence it is concluded that the observed target electron emission is due to target Auger processes.

We identified the Pt target Auger lines by means of atomic structure calculations using the Cowan [17] computer code (Fig. 9). The lines are associated with the

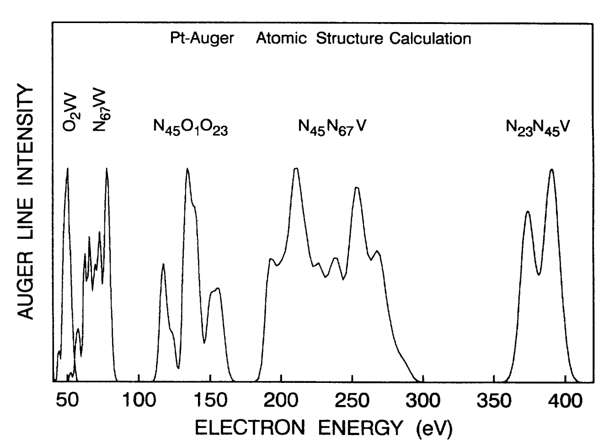

FIG. 9. Pt Auger lines calculated with the COWAN atomic structure code (Ref. [17]). The lines are normalized to the same height.

TABLE II. Electron binding energies as required for the calculation of the diabatic potential curves shown in Fig. 10. The values are taken from a compilation by Williams [19]. All values are in atomic units.

	N K	O K	Ne K	Pt N_1	Pt N_2	Pt N_3	Pt N_4	Pt N_5
$E_M^m(\infty)$	-15.1	-20.0	-32.0	-26.7	-22.4	-19.1	-12.2	-11.6

transitions $N_{23}N_{45}V$ at 370 eV, $N_{45}N_{67}V$ at 220 eV, $N_{45}O_1O_{23}$ at 135 eV, $N_{67}VV$ at 60 eV, and $O_{23}VV$ at 40 eV. Differences between calculated and measured lines are probably due to the neglect of solid-state effects in the calculation.

The $N_{23}N_{45}V$, $N_{45}N_{67}V$, and $N_{45}O_1O_{23}$ target Auger emission is mainly attributed to a vacancy transfer from the projectile K shell to the N shell of the target. This will be shown in the following by using diabatic potential curves and matrix elements obtained within a hydrogenic model proposed by Stolterfoht [18]. Figure 10 shows the diabatic potential curves for the projectile K shell and of Pt target N shells involved in the vacancy transfer as a function of the internuclear separation R, i.e.,

$$E_M^m(R) = E_M^m(\infty) - Q_N(R)/R. \tag{1}$$

The binding energy $E_M^m(R)$ of an electron m belonging to the center M is lowered by the screened Coulomb attraction of the other center N. The effective nuclear charge of center N is given by

$$Q_N(R) = Z_N^n \exp(-\alpha_0 R). \tag{2}$$

The exponential term of Eq. (2) accounts for the fact that more of the nuclear charge at center N is "seen" by an electron at center M the closer the two centers are together. The screening constant α_0 is taken to be

$$\alpha_0 = s(\alpha_{MN})^t, \tag{3}$$

where $\alpha_{MN} = \frac{1}{2}(\alpha_M + \alpha_N)$ with $\alpha_M = \sqrt{2|E_M|}$, $\alpha_N = \sqrt{2|E_N|}$ in atomic units being the "velocity" parameters of the shells of centers M and N involved. In case of the Pt target we choose for E_N the average binding energy of the 18 electrons 4s, 4p, and 4d. For the projectiles we take the binding energies of the K-shell electrons in the neutral atoms. These values taken from a compilation by Williams [19] are listed in Table II. The constants s and t appearing in Eq. (3) have been tabulated by Stolterfoht [18]. We take $s = 0.65$ and $t = 0.5$. In Eq. (2) Z_N^n is the effective nuclear charge due to the screening of all inner shells up to the shell with principal quantum number n. It is obtained by reversing the well-known formula $E^n = Z^2/2n^2$ for the binding energies of the electron of the hydrogen atom:

$$Z_N^n = n\sqrt{2|E_N|} = n\alpha_N. \tag{4}$$

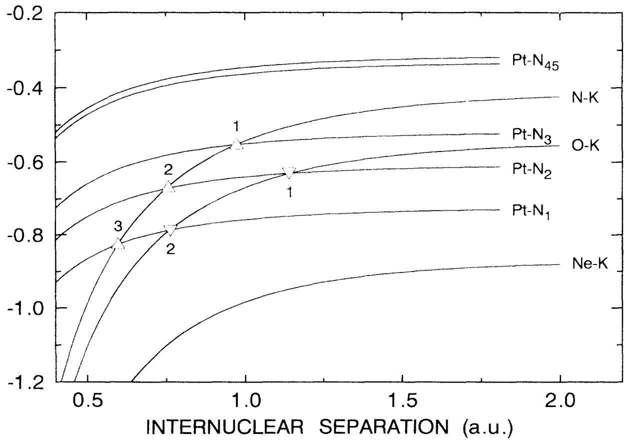

FIG. 10. Diabatic potential curves for the projectiles' K shells and the Pt N shells involved in the K-vacancy transfer (see text).

All values used for the calculation of the diabatic potential curves are listed in Table III. The results for neon, oxygen, and nitrogen interacting with platinum are displayed in Fig. 10. The diabatic potential curve of Pt is shown for O → Pt only. The small deviations of the respective curves for the interaction with nitrogen or neon can be estimated using the parameter α_0 (Table III).

We note diabatic potential curve crossings between the K shell of nitrogen and the N_3, N_2, and N_1 subshells of platinum and between the K shell of oxygen and the platinum N_2 and N_1 subshells. There is no such crossing between the neon K shell and any of the platinum N subshells. It is obvious that the number of crossings depends on the binding energy of the projectile K shell at infinite separation, since during the collison the projectile K shell crosses all those target shells which initially were lower in energy.

At smaller internuclear distances electron promotion can occur. In principle also electron promotion effects could cause a vacancy transfer in the collision. This has been proposed by Havener *et al.* for N^{6+} → Au [20]. The diatomic correlation diagram for the system N → Au shows that eventually the nitrogen K shell is promoted

TABLE III. Parameters used in the calculation of the diabatic potential curves involved in the K-vacancy transfer process. Atomic units are used throughout.

	n	E_N	α_N	α_0
Pt	4	-16.5	5.74	
N	1	-15.1	5.49	1.54[a]
O	1	-20.0	6.32	1.60[a]
Ne	1	-32.0	8.00	1.70[a]

[a] These values refer to the interaction with the Pt N shell.

to the O_{67} subshell of the united atom. The promotion of the nitrogen K vacancy proceeds via the $5f\sigma$ molecular orbital. At some internuclear distance it crosses the $4p\sigma$ molecular orbital which is correlated to the gold N_{45} subshells. It is argued that then a Landau-Zener-type vacancy exchange between these molecular orbitals, i.e., the correlated nitrogen K shell and the N_{45} subshells of gold, leads to the observed emission of Au $N_{45}N_{67}V$ Auger electrons. However, Havener *et al.* [20] do not give the internuclear separation where the proposed crossings between the nitrogen K shell and the gold N_{45} subshells occur. Also the vacancy exchange probability is not estimated. If the crossings occur at too small internuclear separations they cannot be reached, since with the projectile energy used (Havener *et al.* also use 60-keV N^{6+} [20]) the smallest distance of closest approach is 0.13 a.u. This value is the distance of closest approach for a head-on collision.

It should be noted that our interpretation of the target Auger emission differs from Havener *et al.* [20], even though Pt and Au differ in Z only by 1. The vacancy exchange process proposed in this work occurs at rather large internuclear separations R_i (Fig. 10, Table IV). The impact-parameter-dependent probability $p_i(b)$ for a vacancy exchange at crossing i (cf. Fig. 10) can be estimated applying the widely used Landau-Zener formula:

$$p_i(b) = 1 - \exp\left[\frac{-2\pi\,[H_{MN}^{mn}(R_i)]^2}{v\sqrt{1-(b/R_i)^2}\,\Delta F_i}\right] = 1 - \left[1 - p_i(0)\right]^{v/v_i(b)} . \qquad (5)$$

Here

$$v_i(b) = \left.\frac{\partial R}{\partial t}\right|_{R=R_i} = v\sqrt{1-(b/R_i)^2} \qquad (6)$$

is the radial velocity for a straight-line trajectory at the diabatic curve crossing labeled i. In our experiments the projectiles' velocity has been $v = 0.4$ a.u. ΔF_i is the difference of the slopes of the two diabatic potential curves under consideration at $R = R_i$, i.e.,

$$\Delta F_i = \left.\frac{d}{dR}[E_M^m(R) - E_N^n(R)]\right|_{R=R_i} . \qquad (7)$$

For the two-center matrix element $H_{MN}^{mn}(R)$ we take the model matrix element

$$H_{MN}^{mn}(R) = k\alpha_m\alpha_n \exp(-c\alpha_{mn}R), \qquad (8)$$

where $\alpha_m = \sqrt{2|E_M^m(\infty)|}$, $\alpha_n = \sqrt{2|E_N^n(\infty)|}$, $\alpha_{mn} = \frac{1}{2}(\alpha_m + \alpha_n)$ and k and c are tabulated constants [18]. Since Stolterfoht gives values for k and c applicable for the interaction between K and L shells only we use extrapolated values for the interaction between the projectile K and the target N shells, i.e., $k = 3.7$ and $c = 0.84$.

The probabilities $p_i(0)$ estimated along the lines described above are listed in Table IV. They only account for a single passage through a given Landau-Zener crossing. But in our situation, however, there is more than one crossing and each crossing is passed twice, first when the projectile comes in and second when the projectile goes out. In this situation the double-passage vacancy-exchange probability $P_i(b)$ for a given crossing i can be calculated from the single-passage probabilties $p_i(b)$ according to a multicrossing formula given by Salop and Olson [21]. For a system with three crossings it reads

$$\begin{aligned} P_1(b) &= 2p_1(1-p_1)[1 - p_2 + p_2^2(1 - p_3 + p_3^2)] , \\ P_2(b) &= 2p_1p_2(1-p_2)(1 - p_3 + p_3^2) , \\ P_3(b) &= 2p_1p_2p_3(1-p_3) . \end{aligned} \qquad (9)$$

The labeling of the curve crossings refers to Fig. 10. Formulas for systems with only two crossings or one can be obtained by simply setting $p_3 = 0$ and $p_2 = 0$, respectively. The number X of crossings to be taken into account depends on the projectile target combination and on the distance $R_{\min}$ of closest approach which is reached during the collision. The single-collision vacancy-exchange probability is given by the sum over the relevant double-passage vacancy-exchange probabilities [cf. Eq. (9)], i.e.,

$$P^{(1)}(R_{\min}, b) = \sum_{i=1}^{X(R_{\min})} P_i(b) \quad \text{with } p_i(b) = 0 \text{ for i } > X(R_{\min}) . \qquad (10)$$

While the ion penetrates the solid multiple collisions with different target atoms occur. Each of these collisions contributes with nonzero probability to the vacancy exchange only when it fulfills the condition $R_{\min} < R_i^{\max}$. $R_i^{\max}$ is the maximum value of R_i for the collision system under consideration (cf. Table IV). The probability that the vacancy exchange has taken place after j such

TABLE IV. Parameters and results of the calculations of Landau-Zener K-vacancy exchange probabilities. Atomic units are used throughout.

	i[a]	R_i	ΔF	H_{MN}^{mn}	$p_i(0)$
N K - Pt N_3	1	0.97	10.4	0.94	0.74
N K - Pt N_2	2	0.75	21.1	2.51	0.99
N K - Pt N_1	3	0.59	37.4	5.15	1.00
O K - Pt N_2	1	1.15	6.0	0.27	0.17
O K - Pt N_1	2	0.76	19.5	1.84	0.93

[a] The labeling refers to Fig. 10.

TABLE V. K-vacancy exchange probabilities as a function of the glancing angle of incidence ψ obtained from the model calculations. For convenience also the velocity component $v_\perp$ perpendiclar to the surface is given.

		60-keV N → Pt(110)		70-keV O → Pt(110)	
ψ	$v_\perp$(a.u.)	$\langle j\rangle$	$\langle P^{(j)}\rangle$	$\langle j\rangle$	$\langle P^{(j)}\rangle$
10°	0.07	1.74	0.27	3.12	0.68
20°	0.14	1.66	0.31	2.41	0.61
30°	0.20	0.79	0.16	1.13	0.38
45°	0.28	0.60	0.13	0.87	0.28
60°	0.35	0.55	0.12	0.81	0.28
90°	0.40	0.19	0.04	0.37	0.12

collisions is denoted by $P^{(j)}$. The vacancy exchange can only then occur in the jth collision if it has not occurred in the $j-1$ collisons before. Thus $P^{(j)}$ can be expressed in terms of $P^{(j-1)}$ as follows:

$$P^{(j)} = P^{(j-1)} + (1 - P^{(j-1)})P^{(j)}(R_{\min}, b)\,. \qquad (11)$$

Here $P^{(j)}(R_{\min}, b)$ denotes the single-collision vacancy-exchange probability of the jth collision with $R_{\min} < R_i^{\max}$.

We have modeled the ion solid interaction by applying the MARLOWE computer code [22]. For each collision of a projectile with a target atom the values for $R_{\min}$ and b are recorded and used for the calculation of the single-collision probability via Eq. (10). The projectile is traced as long it has not penetrated beyond a certain depth, which we choose to be identical to the escape depth of the target Auger electrons of interest. For 100–250 eV electrons this depth is about 7 Å [10]. At this point the projectile has taken part in j collisions fulfilling the condition for vacancy exchange. The respective probability is then given by $P^{(j)}$. Average values $\langle j\rangle$ and $\langle P^{(j)}\rangle$ over 1000 60-keV N and 70-keV O projectiles for different glancing angles ψ are listed within Table V. As a target a Pt(110)(1 × 1) surface has been specified. The azimuthal direction has been random, i.e., $\phi = 18°$ with respect to the $[1\bar{1}0]$ direction.

The results of our calculations (cf. Table V) support the proposed vacancy-exchange mechanism. The numbers given are considered as first estimates. The competing projectile KLL Auger process diminishes the number of projectile K vacancies available for the Pt target Auger emission. This coupling of the projectile and the target emission is supported by the experimentally observed dependence of the respective electron yields on the ion impact angle (Fig. 7). This effect has not been taken into account in our calculations so far.

V. CONCLUSIONS

The proposed K vacancy-exchange process accounts for the difference in the $N_{45}N_{67}V$ and $N_{45}O_1O_{23}$ target Auger emission between Ne^{9+} on the one hand and N^{6+} and O^{7+} on the other hand. It also accounts for the observed weak Pt $N_{23}N_{45}V$ transition observed in the O^{7+} spectra [Figs. 5(b) and 7], since the vacancy transfer is into the Pt N_1, N_2, or N_3 subshells. In the N^{6+} spectra the Pt $N_{23}N_{45}V$ transition at 370 eV cannot be distinguished because N KLL Auger electrons are also emitted with this energy. The vacancy-transfer mechanism also gives a straightforward explanation for the variation of intensity with angle of incidence. Since both the Pt Auger and the projectile KLL Auger emission are tied to the survival of the K-shell hole of the projectile, it is obvious that the intensity of both emissions should decrease with increasing glancing angle. This is simply because the penetration depth of the projectiles increases with increasing glancing angle, but the escape depth of the Auger electrons is limited to a few a.u. [10].

The vacancy-transfer mechanism found in our experiments excludes total deexcitation of the projectiles in front of the surface. In such a case no K vacancy would be available for any target Auger emission. Incomplete deexcitation of the projectiles in front of the surface has already been inferred, e.g., by Zeijlmans van Emmichoven *et al.* [13]. Since we observe target Auger emission and projectile KLL emission it is obvious that the K vacancies are filled in appreciable numbers within the escape depth of the electrons. However, for larger perpendicular velocities the electron yield of the target Auger emission and the projectile KLL emission decreases significantly. Assuming that for $\psi = 90°$ almost all K vacancies are filled beyond the escape depth of the electrons we arrive at an estimate for the survival time t of the K vacancy within the solid. It is just the escape depth (7 Å) of the electrons divided by the projectile velocity (0.4 a.u.), i.e., $t = 8 \times 10^{-16}$ s.

In case of the Pt $O_{23}VV$ and $N_{67}VV$ Auger lines at 40 eV and 60 eV the experimental facts are in agreement with previous findings [14, 15] of target Auger emission by ion bombardment, i.e., it is concluded that ionization occurs in a violent projectile-target collision which promotes target electrons to such an energy where they can be transferred to vacuum levels.

ACKNOWLEDGMENTS

We gratefully acknowledge the generous assistance of the staff of the ECR source test bench at GANIL. This research was supported in part by the Bundesministerium für Forschung und Technologie and by the Stifterverband für die Deutsche Wissenschaft.

---

* Also at the Hahn-Meitner Institut, D-1000 Berlin 39, Germany.

[1] D. M. Zehner, S. H. Overbury, C. C. Havener, F. W. Meyer, and W. Heiland, Surf. Sci. **178**, 359 (1986).

[2] S. T. de Zwart, Ph.D. thesis, University Groningen, 1987 (unpublished); S. T. de Zwart, Nucl. Instrum. Methods B **23**, 239 (1987).

[3] P. Varga, Appl. Phys. A **44**, 31 (1987).

[4] H. J. Andrä, Nucl. Instrum. B **43**, 306 (1989); H. J. Andrä, in *Proceedings of the 17th International Conference on the Physics of Electronic and Atomic Collisions, Brisbane, 1991*, edited by W. R. MacGillivray, I. E. McCarthy, and M. C. Standage (IOP, Bristol, 1991).

[5] F. W. Meyer, C. C. Havener, S. H. Overbury, K. J. Reed, K. J. Snowdon, and D. M. Zehner, J. Phys. (Paris) **50**, C1-263 (1989).

[6] F. W. Meyer, S. H. Overbury, C. C. Havener, P. A. Zeijlmans van Emmichoven, and D. M. Zehner, Phys. Rev. Lett. **67**, 723 (1991).

[7] S. T. de Zwart, A. G. Drentje, A. L. Boers, and R. Morgenstern, Surf. Sci. **217**, 298 (1989).

[8] R. Köhrbrück, K. Sommer, J. P. Biersack, J. Bleck-Neuhaus, S. Schippers, P. Roncin, D. Lecler, F. Fremont, and N. Stolterfoht, Phys. Rev. A **45**, 4653 (1992).

[9] A. Niehaus, Comments At. Mol. Phys. **9**, 153 (1980).

[10] M. P. Seah and W. A. Dench, Surf. Interface Anal. **1**, 2 (1979).

[11] W. Heiland and E. Taglauer, in *Methods of Experimental Physics*, edited by R. L. Park and M. G. Lagally (Academic, New York, 1985), Vol. 22, p. 299.

[12] A. Itoh, T. Schneider, G. Schiwietz, Z. Roller, H. Platten, G. Nolte, D. Schneider, and N. Stolterfoht, J. Phys. B **16** 3965 (1983).

[13] P. A. Zeijlmans van Emmichoven, C. C. Havener, and F. W. Meyer, Phys. Rev. A **43**, 1405 (1991).

[14] R. Baragiola, in *Inelastic Particle-Surface Collisions*, edited by E. Taglauer and W. Heiland, Springer Series in Chemical Physics Vol. 17 (Springer, Berlin, 1981), p. 38.

[15] A. Oliva, A. Bonanno, M. Camarca, and F. Xu, Nucl. Instrum. Methods B **58**, 333 (1991).

[16] R. Köhrbrück *et al.* (unpublished).

[17] R. D. Cowan, *The Theory of Atomic Structure and Spectra* (University of California Press, Berkeley, 1981)

[18] N. Stolterfoht, in *Progress in Atomic Spectroscopy Part D*, edited by H. J. Beyer and H. Kleinpoppen (Plenum, New York, 1987), p. 415.

[19] G. P. Williams, *Electron Binding Energies for the Elements* (Brookhaven National Laboratory, Upton, NY, 1983).

[20] C. C. Havener, K. J. Reed, K. J. Snowdon, D. M. Zehner, and F. W. Meyer, Rad. Eff. Def. Solids **109**, 99 (1989).

[21] A. Salop and R. E. Olson, Phys. Rev. A **13**, 1312 (1976).

[22] M. T. Robinson and I. M. Torrens, Phys. Rev. B **9**, 5008 (1974); M. Hou and M. T. Robinson, Appl. Phys. **17**, 371 (1978).